JGR Space Physics

RESEARCH ARTICLE
10.1029/2020JA028326

Observations of Density Cavities and Associated Warm Ion Flux Enhancements in the Inner Magnetosphere

C. P. Ferradas[1,2], S. A. Boardsen[1,3], M.-C. Fok[1], N. Buzulukova[1,4], G. D. Reeves[5,6], and B. A. Larsen[5,6]

[1]NASA Goddard Space Flight Center, Geospace Physics Laboratory, Greenbelt, MD, USA, [2]Department of Physics, Catholic University of America, Washington, DC, USA, [3]Goddard Planetary Heliophysics Institute, University of Maryland, Baltimore County, MD, USA, [4]Department of Astronomy, GPHI, University of Maryland, College Park, MD, USA, [5]ISR-1 Space Science and Applications, Los Alamos National Laboratory, Los Alamos, NM, USA, [6]Space Sciences Division, The New Mexico Consortium, Los Alamos, NM, USA

Key Points:

- Density cavities are often observed in the total electron density profiles inside geosynchronous orbit
- Enhancements of warm ion fluxes concurrent with the density cavities are observed with a clear species dependence
- The warm ion flux enhancements associated with the density cavities are likely evidence of the mixing of multiple plasma populations

Correspondence to:
C. P. Ferradas,
cristian.ferradasalva@nasa.gov

Citation:
Ferradas, C. P., Boardsen, S. A., Fok, M.-C., Buzulukova, N., Reeves, G. D., & Larsen, B. A. (2021). Observations of density cavities and associated warm ion flux enhancements in the inner magnetosphere. *Journal of Geophysical Research: Space Physics*, *126*, e2020JA028326. https://doi.org/10.1029/2020JA028326

Received 8 JUN 2020
Accepted 8 FEB 2021

Abstract We present a statistical study of density cavities observed in the inner magnetosphere by the Van Allen Probes during four one-month periods: February 2013, July 2013, January 2014, and June 2014. These periods were chosen to allow the survey of all magnetic local times. We find that density cavities are a recurrent feature of the density profiles of in situ measurements in the inner magnetosphere. We further investigate the correlation between the density cavities and the enhancement of fluxes of warm ions with energies of 10–100 eV. The results show that warm ion flux enhancements associated with the density cavities were observed more frequently for H^+, then for He^+ and the least frequently for O^+. The occurrences of the associated flux enhancements were increased when considering only the cavities inside the plasmasphere. Possible mechanisms responsible for the observed warm ion flux enhancements and the role of density cavities on these ion flux enhancements are discussed.

Plain Language Summary The electron density measured in the Earth's inner magnetosphere often exhibits cavity-like structures in the form of local dips in their profiles. We present a statistical study of such density cavities, observed by the Van Allen Probes mission during four one-month periods, which cover all magnetic local times. We investigate the observation of these cavities in relation to the concurrent observation of enhanced fluxes of ions with energies of 10–100 eV. We find that this relationship is not the same for all types of ions: enhanced ion fluxes are more frequently observed for H^+, then for He^+, and finally for O^+ in association with the density cavities. When considering this relationship only inside the dense region of cold plasma, inside the plasmasphere, the correlations were increased. We discuss possible mechanisms responsible for the observed enhancement of ion fluxes.

1. Introduction

A variety of magnetospheric missions have surveyed the plasmasphere environment, finding and describing a multitude of density structures. Some of the density structures have been described as plasmaspheric plumes (e.g., Goldstein et al., 2014), notches (e.g., Burch et al., 2004; Gallagher et al., 2005), plasmaspheric density troughs or cavities (Carpenter et al., 2000; Horwitz et al., 1990), plasmasphere shoulders (e.g., Pierrard & Cabrera, 2005), and crenulations (e.g., Spasojević, 2003). These structures are determined by the time history of geomagnetic activity, as are the general configuration, size, morphology and composition of the plasmasphere. Even though these density structures, as well as the relationship between the plasmasphere and other populations in the inner magnetosphere, have been widely studied for decades (e.g., Gurgiolo et al., 2005 and references therein), the relationship between density structures and the more energetic populations in the inner magnetosphere have been understudied.

Being the signatures of changing geomagnetic conditions, density structures are often observed in, though not limited to, the outer plasmasphere (Darrouzet et al., 2009; Moldwin et al., 1995 and references therein). In contrast to the inner plasmasphere, where densities are high (above ~100 cm^{-3}), temperatures are cold (~1 eV) and ions exhibit isotropic and/or pancake pitch angle distributions (PADs, e.g., Horwitz & Chappell, 1979; Nagai et al., 1983), the outer plasmasphere is less dense, contains a warmer plasma component, and ions often exhibit field-aligned PADs (e.g., Baugher et al., 1980; Chappell, 1982; Lennartsson

& Reasoner, 1978). At distances typically outside the plasmasphere lies the warm plasma cloak, which is composed of less dense (below 1 cm^{-3}) and warmer plasma (>∼10 eV) and ions mainly exhibit field-aligned PADs. There is not, however, a distinct nor abrupt separation between the plasmasphere plasma and the cloak plasma but instead, rather often overlap and mixing between these regions is observed concurrently with fine density structures in the outer plasmasphere (e.g., Chappell, 1982; Horwitz & Chappell, 1979; Moldwin et al., 1995). This coexistence of plasmasphere-like and cloak-like plasma has been demonstrated by the observation of mixed ion PADs. Early missions like ATS-6, SCATHA, and ISEE-1 observed species dependent PADs (Baugher et al., 1980; Horwitz et al., 1981; Nagai et al., 1983). For example, Baugher et al. (1980) reported observations made with the ISEE-1 mission of field-aligned O^+ coexisting with He^+ with pancake PAD and H^+ with a combination of pancake and isotropic PAD. Similarly, observations from the ATS-6 mission at geosynchronous orbit have shown multiple examples of mixed PADs for different ion species, most commonly pancake and field-aligned PADs (Chappell, 1982; Horwitz & Chappell, 1979). All this evidence indicates that the outer plasmasphere is a complex region where fine-scale density structure, mixing of different plasma populations and mass dependent dynamical processes that energize plasma of ionospheric origin in distinct directions relative to the background magnetic field are often observed. Furthermore, as a result of the important and complex interactions between plasmas from the cold plasmasphere and hot plasma sheet and ring current taking place in the vicinity of the plasmapause, where these populations often overlap, the latter is often viewed as a boundary layer, namely the plasmasphere boundary layer (PBL, Carpenter & Lemaire, 2004).

Moreover, recent studies have shown that density structures can lead to local increases of the index of refraction, which can favor the trapping of magnetosonic (MS) waves (e.g., Ma et al., 2014; Yue et al., 2020). MS waves are linearly polarized electromagnetic emissions typically between the proton gyrofrequency and the lower hybrid resonance frequency (e.g., Laakso et al., 1990; Santolík et al., 2004) that are observed near the magnetic equator (e.g., Santolík et al., 2002). They are excited by the free energy provided by ∼1–30 keV ions exhibiting ring distributions (e.g., Boardsen et al., 1992; Chen et al., 2011; Horne et al., 2000; Perraut et al., 1982; Thomsen et al., 2011) and are able to interact with radiation belt particles (e.g., Bortnik & Thorne, 2010; Mourenas et al., 2013; Xiao et al., 2014) as well as with cold ions (e.g., Hill et al., 2020; Horne et al., 2000; Sun et al., 2017; Yuan et al., 2018). Even though other types of waves, such as electromagnetic ion cyclotron (EMIC) waves, are also known to interact with cold ions and cause heating (e.g., Ma et al., 2019; Mouikis et al., 2002; Young et al., 1981; Zhang et al., 2011), recent studies have highlighted the occurrence of MS waves inside density cavities and the ability of this wave mode to energize cold ions. More specifically, three recent studies have reported the first direct observations of cold ion heating by interaction with MS waves inside density cavities (Hill et al., 2020; Ma et al., 2019; Yuan et al., 2018). These studies suggest that cold ion heating by MS waves could be expected to occur favorably in plasmaspheric density cavities due to the lower background plasma density, which can modulate the wave growth rates (Yuan et al., 2017). These results further suggest that density cavities can play a more important role in the interaction between cold plasma and warmer populations, like the warm plasma cloak, than previously thought.

In this study, we perform a statistical study of density cavities observed in the electron density profiles from the Electric and Magnetic Field Instrument Suite and Integrated Science (EMFISIS) instrument (Kletzing et al., 2013) onboard Van Allen Probes (also referred to by its previous name, Radiation Belts Storm Probes) A (RBSP-A, Mauk et al., 2013) during four one-month periods. The correlation between the observation of density cavities and warm ion flux enhancement (WIFE) of H^+, He^+, and O^+ is established by examination of the ion fluxes in the energy range of 10–100 eV measured by the Helium, Oxygen, Proton, Electron (HOPE) mass spectrometer (Funsten et al., 2013) in the Energetic Particle, Composition, and Thermal Plasma (ECT) suite (Spence et al., 2013). We further investigate the occurrence of MS wave activity concurrent with the density cavities and discuss possible mechanisms responsible for the WIFE events, including wave-particle interactions with MS waves.

2. Data Analysis

This study consists of data analysis of electron density measurements from the EMFISIS level 4 data files and ion flux measurements from the HOPE level 3, release-04 data files obtained by RBSP-A. In the following subsections, we detail the methodology of the analysis for the identification of density cavities,

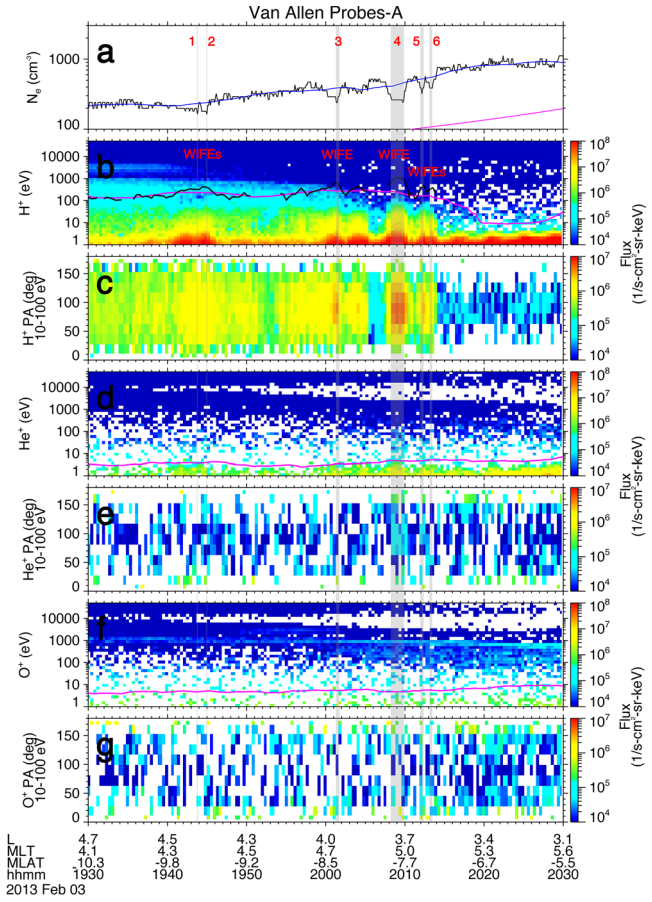

Figure 1. Plasma measurements from RBSP-A at 1930–2030 UT on 3 February 2013. (a) Total electron density from EMFISIS, energy-time spectrograms of (b) H^+, (d) He^+, and (f) O^+ differential flux, and pitch angle-time spectrograms of (c) H^+, (e) He^+, and (g) O^+ differential flux for the energy range of 10–100 eV observed by ECT/HOPE. The magenta curve overplotted in panel a corresponds to the density function $10 \times \left(6.6 / L\right)^4\ cm^{-3}$, which serves as a proxy of the location of the spacecraft with respect to the plasmasphere. The blue curve overplotted in panel a is the total electron density smoothed in time using a smoothing window of 10 min. The black curve overplotted in panel b is the H^+ integrated flux divided by 10^5 over the energy range of 10–100 eV. The magenta curves overplotted in panels b, d, and f are the H^+, He^+, and O^+ integrated fluxes divided by 10^5 and smoothed in time using a smoothing window of 10 min, respectively. The six periods shaded in gray and labeled in panel a indicate the observation of density cavities. The density cavities that exhibit associated H^+ warm ion flux enhancements (WIFEs) are marked with "WIFE" in panel (b). ECT, Energetic Particle, Composition, and Thermal Plasma; EMFISIS, Electric and Magnetic Field Instrument Suite and Integrated Science; HOPE, Helium, Oxygen, Proton, Electron; RBSP-A, Radiation Belts Strom Probes-A.

associated warm ion flux enhancement (WIFE), and magnetosonic (MS) wave activity.

2.1. Observations of Density Cavities

The electron density used in this study is estimated from the upper hybrid resonance frequency detected by the EMFISIS high-frequency receiver (HFR). We define a density cavity as a significant depletion (as defined below) embedded in a larger density structure. Density cavities can be associated with or contained within a variety of meso and macro-scale density structures as those discussed above. To efficiently analyze the large data set provided by the Van Allen Probes measurements and to maximize the accuracy of the analysis, we developed an automated algorithm to identify the density cavities in the EMFISIS density profiles. The criterion used by the algorithm to identify density cavities is based on the simple criterion used by Horwitz et al. (1990), by which cavities were at least a factor lower than the surrounding density (see density profile pattern *D* in Horwitz et al., 1990). Our automated algorithm identified density cavities as follows. In first place, the "surrounding" or "background" density was determined by smoothing the full-resolution density in time over a 10-min smoothing window. Since the motivation for the present study came from the finding that density cavities were often accompanied by the observation of enhanced warm ion fluxes, we first identified several such events and found that their typical duration ranged from a few seconds to a few minutes of observation time. After trying several smoothing window values, we found that a 10-min smoothing window worked well to identify cavities with the desired duration range. Second, the algorithm measured full-resolution density relative to the background (smoothed) density and identified all data points that met a depletion threshold criterion: where the density was lower than 0.75 of the background density, or in other words, where the density was depleted by a factor greater than 25% with respect to the background density. Third, the algorithm then grouped full-resolution density points meeting this depletion criterion together into each "cavity" using the following criterion: two depleted density points must be separated from each other by another density point above the density background or else they are considered part of the same cavity. Fourthly, and last, since we are interested in regions of depleted density and not only in regions of sharp density gradients, such as near the plasmapause, the algorithm discarded a density cavity if the ratio of the density values at its edges exceeded a factor of 5.

Figure 1a shows the full-resolution density from EMFISIS in black and the background (smoothed) density in blue for 1930–2030 UT on February 3, 2013. During this period six density cavities were identified by the automated algorithm, which are labeled and indicated by the gray shaded periods. The corresponding minimum densities inside the cavities were 164, 164, 240, 238, 319, and 387 cm^{-3}, respectively. The magenta curve in Figure 1a corresponds to the density function $10 \times \left(6.6 / L\right)^4\ cm^{-3}$ (e.g., Hartley et al., 2016; Li et al., 2010; Moldwin et al., 1994; Sheeley et al., 2001), which serves as a proxy of the location of the spacecraft with respect to the plasmasphere. According to this criterion, which is described in Section 2.4, the density cavities in Figure 1a were inside the plasmasphere. In similar format, Figure 2a shows the density from EMFISIS during 0045–0115 UT on February 14, 2013. During this period three density cavities were identified and are labeled and are highlighted by the gray shaded periods.

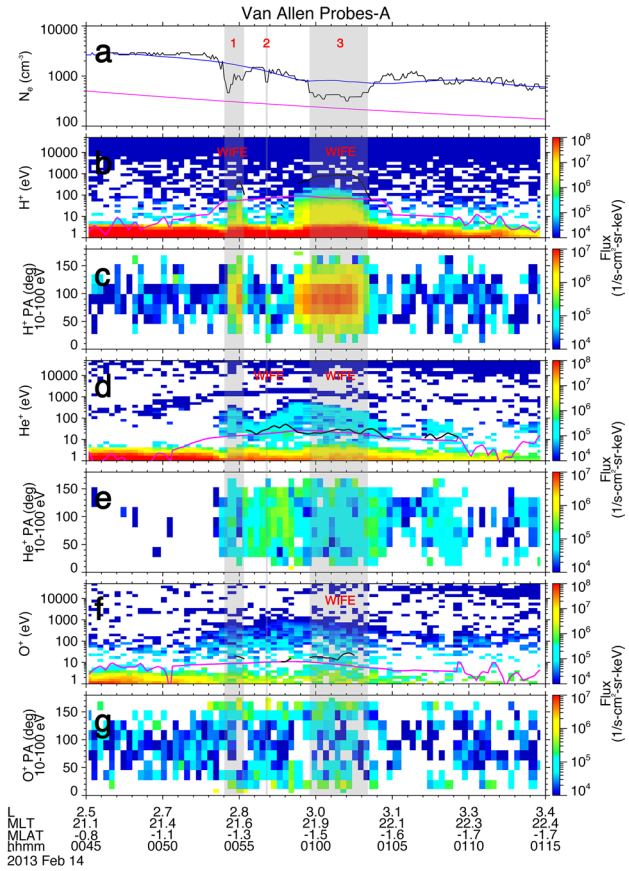

Figure 2. Plasma measurements from RBSP-A at 0045–0115 UT on 14 February 2013 in a similar format as Figure 1. RBSP-A, Radiation Belts Strom Probes-A.

The corresponding minimum densities inside each cavity were 461, 756, and 315 cm^{-3}, and according to the density criterion they were inside the plasmasphere.

2.2. Observations of Associated Warm Ion Flux Enhancement (WIFE) Events

To determine the correlation between the density cavities and warm ion fluxes, we also developed an automated algorithm to identify warm ion flux enhancement (WIFE) events in the HOPE ion flux data. The automated algorithm identified WIFE events as follows. First, the full-resolution integrated flux at energies of 10–100 eV was calculated by adding the fluxes of all HOPE energy channels within this energy range. The integrated flux was then re-binned to the EMFISIS time resolution. We will refer to this as the full-resolution integrated flux. In second place, the "background" integrated flux was determined by smoothing the full-resolution integrated flux in time over a 10-min smoothing window. The 10-min smoothing window was used for consistency with the identification of density cavities. Third, the algorithm measured full-resolution integrated flux relative to the background (smoothed) integrated flux during each cavity period and determined if a cavity event was also a WIFE event according to an enhancement threshold criterion: if at least one integrated flux point was higher than 1.5 of the background integrated flux, or in other words, if the integrated flux was enhanced by a factor greater than 50% with respect to the background integrated flux. Fourthly, to minimize the identification of false positives when fluxes were too low, the algorithm discarded periods when the integrated flux was deemed "too low". The integrated flux was considered too low when it met any or both of two conditions: (1) when its value was below a minimum background threshold of 10^7 or 10^6 $s^{-1}cm^{-2}sr^{-1}$ keV^{-1} for H^+ and for He^+ and O^+, respectively, and (2) when more than one third of the energy bins had zero counts (there are 15 HOPE energy channels between 10 and 100 eV, so this condition was met if at least six channels had zero counts). These minimum background threshold values were empirically determined by eye inspection of the typical flux levels at these energies for the different ion species. This means that WIFE identification required that the enhancement threshold criterion be met and that none of the two conditions for "low flux" be met. In fifth and last place, since HOPE ion fluxes can be affected by spacecraft charging events (Sarno-Smith et al., 2016), the algorithm also identified periods when the spacecraft potential measured by the Electric Field and Waves (EFW) instrument was below −10 V, and discarded them.

Figures 1b and 1c show the energy-time spectrogram of H^+ omnidirectional fluxes for the whole HOPE energy range (1 eV–50 keV) and the pitch angle-time spectrogram of H^+ fluxes for energies of 10–100 eV, respectively. Figures 1d-1e are analogous to Figures 1b-1c but for He^+, and Figures 1f-1g for O^+. The black curve overplotted in Figure 1b is the full-resolution H^+ integrated flux and the magenta curve also overplotted is the background (smoothed) integrated flux. Both have been divided by 10^5 to bring them to scale with the spectrogram. To indicate the periods when the integrated flux was "too low", these periods have not been plotted and appear as gaps in the black curve. Similarly, both integrated flux curves have been overplotted in Figures 1d and 1f for He^+ and O^+, respectively. However, notice that the full-resolution He and O integrated fluxes (black curves) are not plotted. This is because the heavy ion integrated fluxes were too low, below 10^6 $s^{-1}cm^{-2}sr^{-1}$ keV^{-1}, for the entire period plotted. Thus Figure 1 shows that the six density cavities identified during the inbound pass on 1930–2030 UT on 3 February 2013 have associated H^+ WIFE events and none of them have associated He^+ nor O^+ WIFE events.

A noteworthy feature of the warm ions presented in Figure 1 is the species-dependent characteristic of the pitch angle distributions (PADs). Figure 1c indicates that the enhanced warm H^+ exhibit pancake PADs

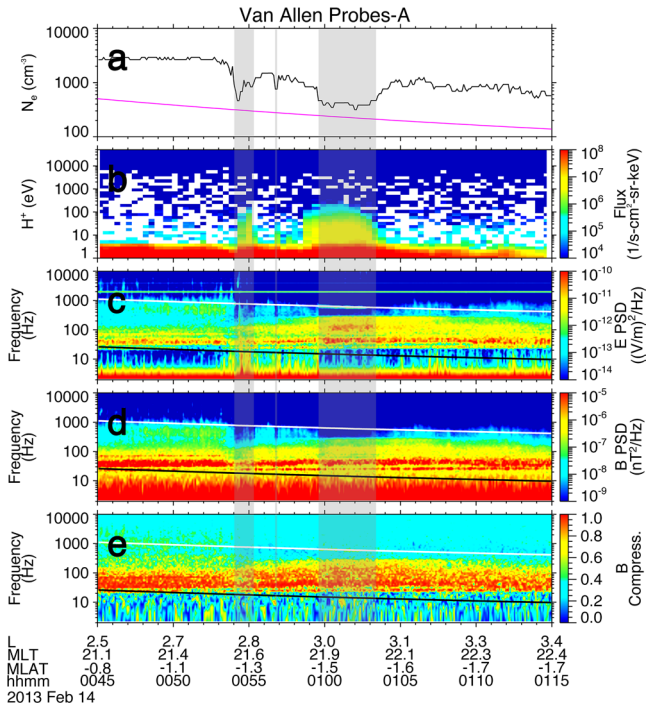

Figure 3. (a) Total electron density from EMFISIS, (b) energy-time spectrogram of H^+ differential flux from ECT/HOPE, frequency-time spectrograms of (c) the sum of the two long spin plane antenna electric field power spectral densities (PSD), of (d) the sum of the three search coil magnetic field PSD, and of (e) the magnetic compressibility from EFW and EMFISIS onboard RBSP-A at 0045–0115 UT on 14 February 2013, the same period displayed in Figure 2. The magenta curve overplotted in panel a corresponds to the density function $10 \times \left(6.6 / L\right)^4\ cm^{-3}$, which serves as a proxy of the location of the spacecraft with respect to the plasmasphere. The black and white curves overplotted in panels c, d, and e are the proton cyclotron and the lower hybrid resonance frequencies, respectively. The three periods shaded in gray indicate the observation of density cavities. ECT, Energetic Particle, Composition, and Thermal Plasma; EFW, Electric field waves; EMFISIS, Electric and Magnetic Field Instrument Suite and Integrated Science; HOPE, Helium, Oxygen, Proton, Electron; RBSP-A, Radiation Belts Strom Probes-A.

(peaked at ∼90) suggesting that these warm protons are trapped. Even during the periods when no cavities were observed, H^+ exhibit mostly pancake PADs. In contrast, and even though the heavy ion warm fluxes are low, Figures 1e and 1g show that He^+ and O^+ exhibit a bidirectional PAD. This bidirectional PAD is more clearly seen in the O^+ fluxes. It is possible that trapped He^+ and O^+ fluxes could have dropped below instrumental background level at the magnetic latitude (MLAT) of the spacecraft (MLAT ∼ −7–−10), as it is expected that trapped ion fluxes with anisotropic PADs drop significantly with increasing MLAT (Olsen et al., 1994). Figure 1 thus portrays a typical pass where six density cavities were observed with associated H^+ WIFE events, the enhancements being observed mainly in the direction perpendicular to the magnetic field.

In a format similar to Figures 1, 2 shows that from the three cavities identified during this period, cavities one and three showed concurrent H^+ WIFE, whereas cavities two and three showed concurrent He^+ WIFE and only cavity three showed O^+ WIFE. Figures 2c and 2e show that the warm H^+ and He^+ ions exhibit pancake PADs, whereas warm O^+ ions have a distinct bidirectional PAD. These PADs are observed both inside and outside the density cavities. Notice that the spacecraft is close to the equator (MLAT ∼ −1) during these observations. These distinct PADs among ion species are not a novel observation for ions with these warm energies in the inner magnetosphere (e.g., Horwitz et al., 1981) and will be discussed further later.

2.3. Observations of Magnetosonic (MS) Waves

We investigate the occurrence of MS wave activity during the density cavity events by employing the survey of the fast MS wave mode with Van Allen Probes EMFISIS observations performed by Boardsen et al. (2016). The criteria for detection of this wave mode was a magnetic compressibility greater than 0.7 and electric and magnetic power spectral densities greater than 2 times the noise floor. For a detailed description of the analysis for the wave detection and the statistical results, see Boardsen et al. (2016). The occurrence of MS wave activity associated with a density cavity was established if a positive identification of this wave mode according to the survey of Boardsen et al. (2016) occurred during the time span of the cavity observation.

Figures 3c–3e show the electric and magnetic power spectral densities and the magnetic compressibility during the same period as Figure 2. The black and white curves overplotted in these panels correspond to the proton cyclotron (f_{CP}) and the lower hybrid resonance (f_{LHR}) frequencies, respectively. The measured values, especially the wave packets with compressibility greater than ∼0.7, show occurrence of MS wave activity clearly seen at frequencies between f_{CP} and f_{LHR} throughout this period; thus, for our statistical analysis, the cavities observed during this period had MS waves associated with them. Even though it is not shown, we note that the period plotted in Figure 1 did not exhibit MS wave activity, and thus the six cavity events shown there are examples of cavities without associated MS waves.

2.4. Statistical Results

We report results based on four one-month periods (February and July 2013, and January and June 2014) of electron density and ion flux measurements from RBSP-A. These four months were chosen to obtain data coverage at all magnetic local times (MLTs). The data coverage, in terms of dwell time in minutes, from RBSP-A is shown in Figure 4a as a function of L shell and MLT. The bin size in Figure 4 is 0.2 L shell

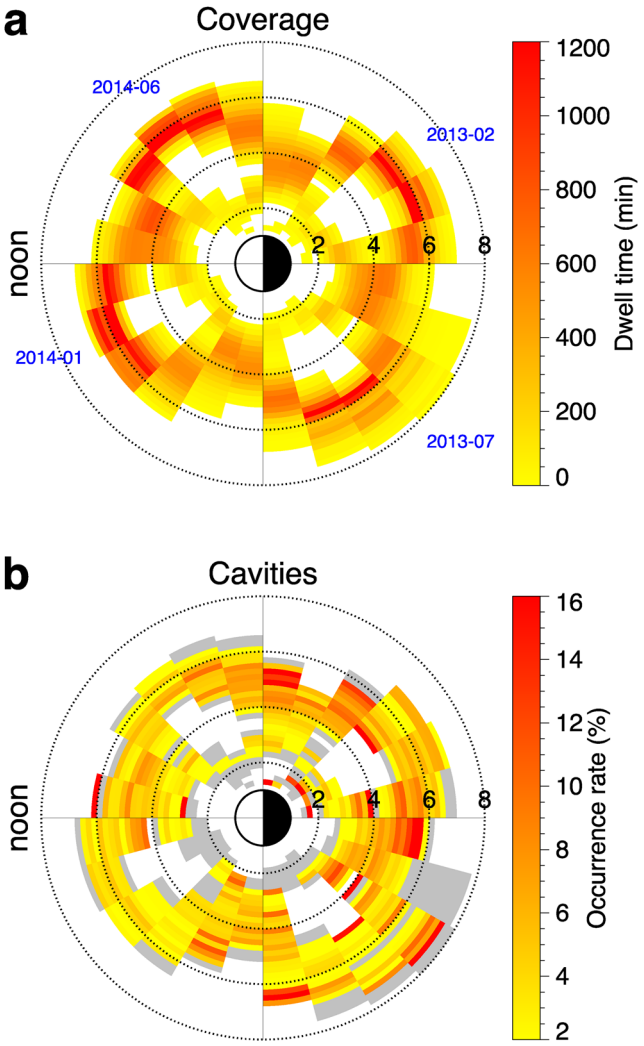

Figure 4. (a) Data coverage of RBSP-A for four one-month periods: February and July 2013 and January and June 2014. (b) Occurrence rate of the density cavities observed by Van Allen Probes-A. The white areas indicate zero dwell time and the gray areas indicate regions where RBSP-A was located but did not observe density cavities. Both quantities are plotted as a function of L shell and magnetic local time. RBSP-A, Radiation Belts Strom Probes-A.

x 1 h of MLT. The L values were computed (throughout this study) using the Tsyganenko and Sitnov empirical model (TS04) (Tsyganenko & Sitnov, 2005). The regions in white denote areas that were not covered by RBSP-A. Figure 4a shows that the spacecraft covered regions mostly inside $L = 6$, except in the dusk-midnight quadrant, were larger L shells were covered. This is due to magnetic field stretching that occurs on the nightside, particularly in the premidnight sector. While all MLTs were covered, not all L values inside $L = 6$ were covered at each MLT. Since the spacecraft orbital speed is significantly reduced around apogee, the regions with most coverage (>1,000 min) correspond to the four sectors were RBSP-A's apogee was located during the four months, namely near $L \sim 6$ and MLT $\sim$ 2, 8, 14, and 20.

Geomagnetic activity as represented by the Kp index was low to moderate ($Kp \leq 4.3$) during February 2013 and January 2014, whereas it was more disturbed during July 2013 and June 2014, with periods reaching $Kp = 5.3$ and $Kp = 6.3$, respectively. Moreover, there was no significant storm activity ($Dst \geq -40\,nT$) during February 2013, and January and June 2014, with three moderate storms ($-100\,nT <$ peak Dst $< -50\,nT$) occurring during July 2013.

2.4.1. Occurrence of Density Cavities

Using our automated algorithm to survey the EMFISIS density data for February and July 2013 and for January and June 2014, a total of 4,561 density cavities were identified, out of which 150 events were not taken into account due to unavailable HOPE measurements in the desired low energy range and 25 due to spacecraft charging events. This means that after discarding the cavity events with no available ion fluxes, we obtained for the present study a total of 4,386 cavity events with available warm ion flux measurements. Figure 4b shows the occurrence rate of density cavities observed by RBSP-A over the four one-month periods. To determine the occurrence rates, the time duration of each density cavity was sorted and summed within each respective bin of L shell and MLT. The occurrence rate is then defined as the total density cavity observation time divided by the total RBSP-A dwell time at each bin. Bins colored in gray indicate areas where RBSP-A surveyed and had density measurements, but no density cavity was observed.

Overall, the occurrence rates are higher on the nightside than on the dayside. The most notable peak occurrence region is the MLT = 21–6 region at L = 3–6, which corresponds to February 2013. Other regions with peak occurrence are found in several "fringing" portions of RBSP-A's coverage, both at low and high L shells, where coverage was relatively low. We, therefore, should be careful interpreting these peak regions as it appears that, in passing through those regions, RBSP-A has had a bit of serendipity and observed a few cavities despite the limited coverage. Comparing the four regions with highest coverage it becomes clear that there is a preferred occurrence of cavities in the midnight-dawn quadrant and a lowest occurrence rate in the afternoon quadrant. This result is consistent with previous observations and will be discussed in the Discussion section.

The occurrence rates of density cavities with and without associated WIFE events are shown for each of the four one-month periods, as well as for the entire period covered in the study, in Figure 5. The number at the top of each period indicates the number of detected density cavities. We note that significantly more cavities were observed during February 2013 (1,763) than during the other three months (June 2014 had

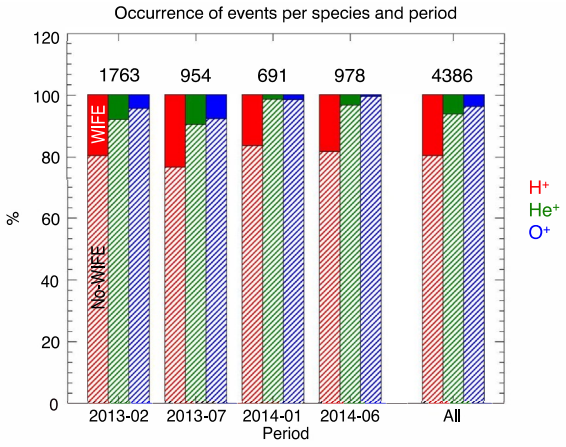

Figure 5. Histogram showing the occurrence rates of density cavities with (solid color bars) and without (striped color bars) associated warm ion flux enhancement (WIFE) per ion species. The occurrence rates are shown for each of the four one-month periods covered in the study as well as for the total time. The total number of density cavities detected in each period is indicated at the top.

the second most with 978). The reason for this high occurrence of density cavities during February 2013 seems not to be related to geomagnetic activity since geomagnetic conditions during this month were comparable to those during January and June 2014. This high occurrence might be more related to the MLT sector where RBSP-A surveyed during this period.

In an attempt to sort the cavity observations in terms of the higher-density plasmasphere and the lower-density trough-like region, we use a density criterion that has been widely used (e.g., Hartley et al., 2016; Li et al., 2010; Moldwin et al., 1994; Sheeley et al., 2001). According to this criterion, the spacecraft is considered to be inside the plasmasphere if the measured plasma density is higher than the larger of the two density functions 30 and $10 \times \left(6.6 / L\right)^4$ cm^{-3}, the spacecraft is considered to be outside the plasmasphere if the plasma density is lower than the smaller of these two functions, and the region where the plasma density has values between these two functions defines the plasmapause region. Using this criterion with the minimum density inside a cavity and the corresponding location of the spacecraft as indicative of the density and the L value of each cavity, we find that out of the 4,386 observed density cavities, 2,308 (52%) were observed inside the plasmasphere, 1,568 (36%) were observed outside the plasmasphere, and 510 (12%) in the plasmapause region.

2.4.2. Correlation Between Density Cavities and WIFEs

Of special interest is the species dependence of the WIFE events. Therefore, for all detected density cavities, we identified cavities that exhibited a H^+, He^+, and O^+ WIFE as described in Section 2.2. The occurrence rates in Figure 5 show that the majority of density cavities did not exhibit concurrent WIFE. Overall, WIFE events were observed most frequently for H^+, then for He^+ and the least frequently for O^+. Out of the 4,386 density cavities detected, 866 (20%) exhibited associated H^+ WIFE, whereas 277 (6%) and 170 (4%) exhibited associated He^+ and O^+ WIFE, respectively. Moreover, July 2013 showed the highest WIFE occurrence rates for all ion species, with 23%, 10%, and 8% occurrence rates for H^+, He^+, and O^+, respectively. This month the rates were particularly higher for the heavy ions. This can be related to storm activity since three storms occurred during this month, whereas no storm occurred during the other three months.

Figure 6 shows the occurrence rates of H^+, He^+, and O^+ WIFE events as a function of L shell and MLT. Overall, there are higher occurrence rates on the nightside than on the dayside for all ion species, similar to the distribution of cavities in Figure 4b. Figure 6a shows that there are H^+ WIFE events observed at all MLTs, with a region of high occurrence near midnight at $L \sim 3$–5. Figures 6b and 6c show particularly low occurrence rates on the nightside, with the lowest rates in the afternoon and prenoon quadrants for He^+

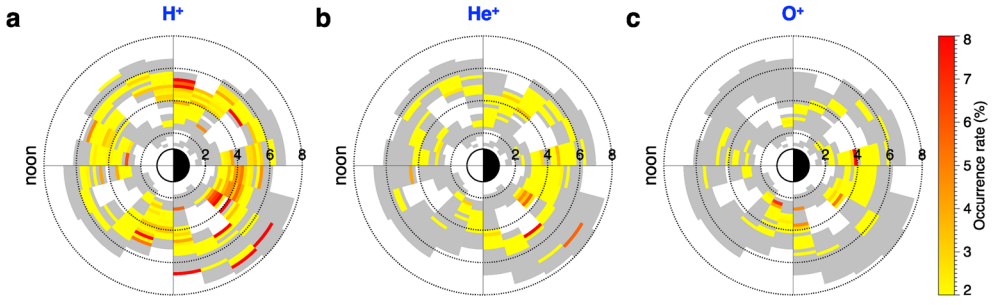

Figure 6. Occurrence rates of density cavities with associated (a) H^+, (b) He^+, and (c) O^+ warm ion flux enhancements (WIFEs).

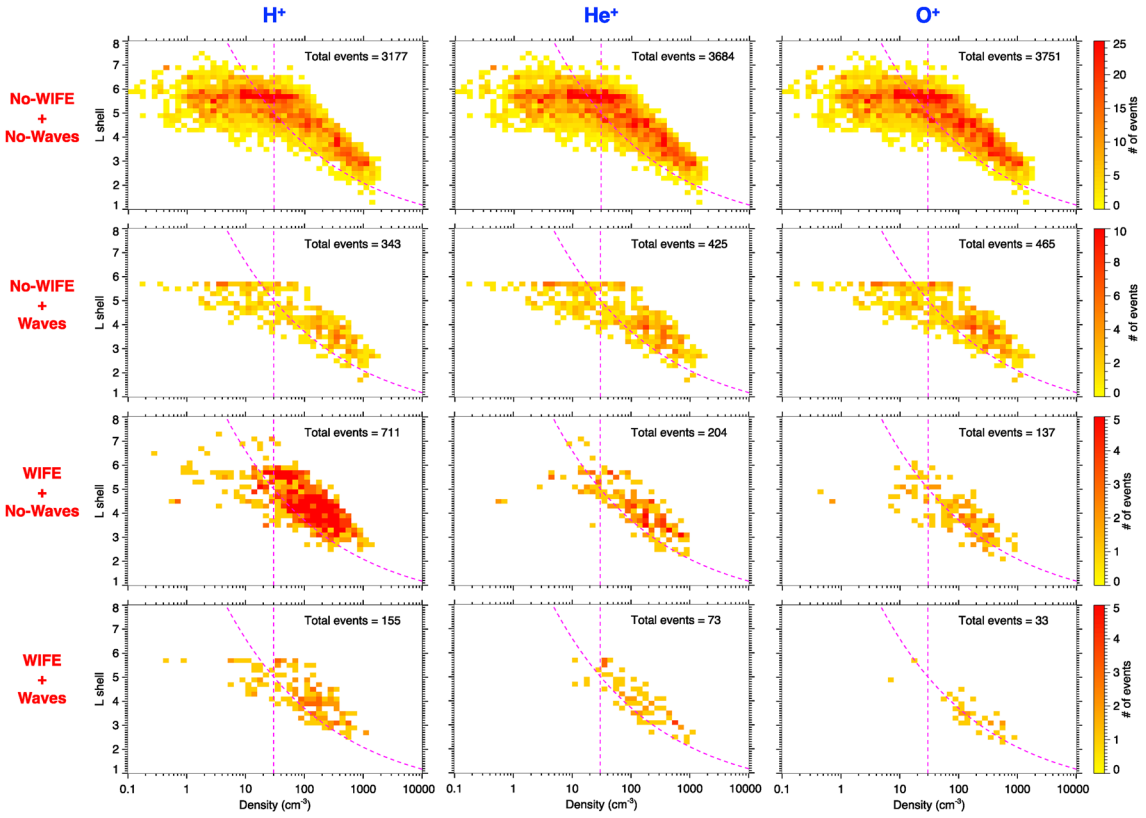

Figure 7. The distribution of the density cavities with respect to density and L shell. The density cavity events are sorted by the concurrent observation, or the lack thereof, of associated warm ion flux enhancement (WIFE) and magnetosonic (MS) wave activity into four groups (rows): No WIFE and no waves, no WIFE and waves, WIFE and no waves, and WIFE and waves. The three columns correspond to the three ion species: H^+, He^+, and O^+. White bins indicate no events.

and O^+ WIFEs, respectively. Figure 6c indicates that most O^+ WIFE occurrence was observed in the region of MLT ~ 16–01 inside $L \sim 5$.

If we consider only the density cavities observed inside the plasmasphere, out of 2,308, 655 (28%) showed associated H^+ WIFE, whereas 210 (9%) and 97 (4%) showed associated He^+ and O^+ WIFE, respectively. Thus, the occurrence rates of cavities with associated H^+ and He^+ WIFE increase inside the plasmasphere, whereas for O^+ they remain the same. On the other hand, if we consider the preferred region for WIFE occurrence, we find that out of 866 H^+ and 277 He^+ WIFE events, 76% were observed inside the plasmasphere for both lighter ions, whereas from 170 O^+ WIFE events, only 57% were observed inside the plasmasphere. This indicates a similar preferred occurrence of H^+ and He^+ WIFEs inside the plasmasphere, whereas for O^+ WIFEs this preference is not so clear.

2.4.3. Correlation Between Density Cavities with WIFEs and MS Waves

To further investigate the correlation between the WIFEs and the occurrence of MS waves, Figure 7 shows the distributions of all cavity events as a function of density and L shell. For each cavity, the minimum density inside the cavity and its corresponding L value have been used. The cavities have been sorted by the three ion species and into four groups by the occurrence, or lack thereof, of associated WIFE and MS wave activity. In each panel, the two density functions 30 and $10 \times \left(6.6 / L\right)^4$ cm^{-3} are overplotted in magenta dashed lines. White bins indicate no events and the total number of cavity events in each group is indicated on the upper right corner of the respective panel. The distributions show that MS wave activity is observed over a wide range of densities and L values, though most cases are observed inside the plasmasphere. Moreover, for all species most WIFE events were not concurrent with MS waves. Out of the 866 H^+ WIFE events,

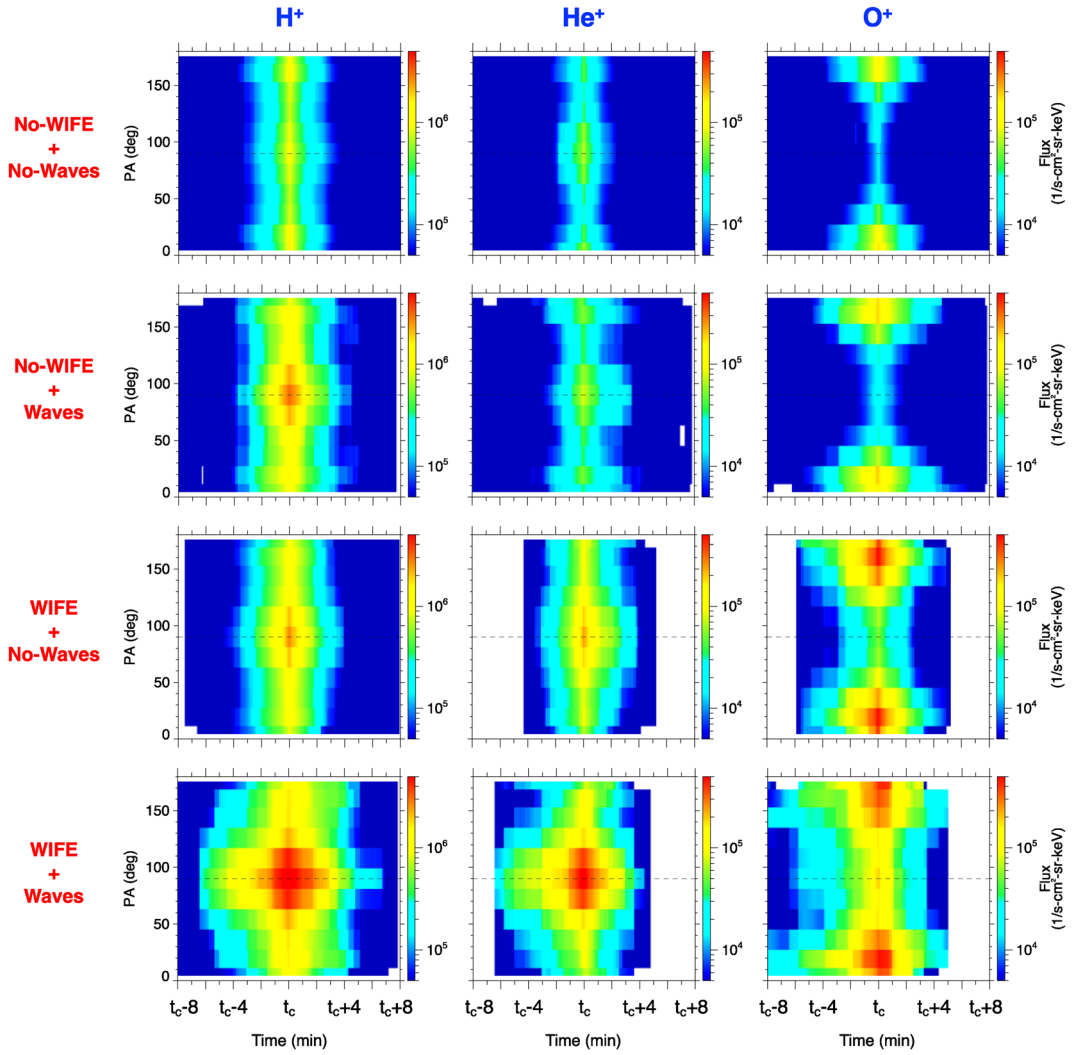

Figure 8. Superposed epoch analysis of the pitch angle distributions (PADs) of warm ion fluxes for each density cavity centered at the time of minimum density. For each ion species, the PADs are sorted into the four types of events identified in Figure 7.

only 155 (18%) had associated MS wave activity, and from the 277 and 170 He^+ and O^+ WIFE events, only 73 (26%) and 33 (19%), respectively, had associated MS wave activity.

Figure 8 shows a superposed epoch analysis of the pitch angle distributions (PADs) of 10–100 eV ions for the four types of events identified in Figure 7. For the superposed epoch analysis, the pitch angle-time flux spectra used for each group consisted of the full duration of every cavity event time shifted to the reference time, t_c, the time of minimum density inside the cavity. The plotted fluxes correspond to the mean flux for each pitch angle-time bin. We first discuss the cavity events with no associated WIFE (two top rows). It is important to note that the PADs for different ion species are different. In the absence of MS waves, the H^+ PAD shows a bidirectional component accompanied by a weaker perpendicular component (peaked at 90), whereas when MS waves are present, the perpendicular component is significantly enhanced and the bidirectional component remains approximately the same. The He^+ PAD without MS waves exhibits a bidirectional component accompanied by a stronger perpendicular component, and when MS waves are present, again, the perpendicular component is enhanced. The O^+ PADs, on the other hand, are strongly bidirectional both in the presence and absence of MS waves.

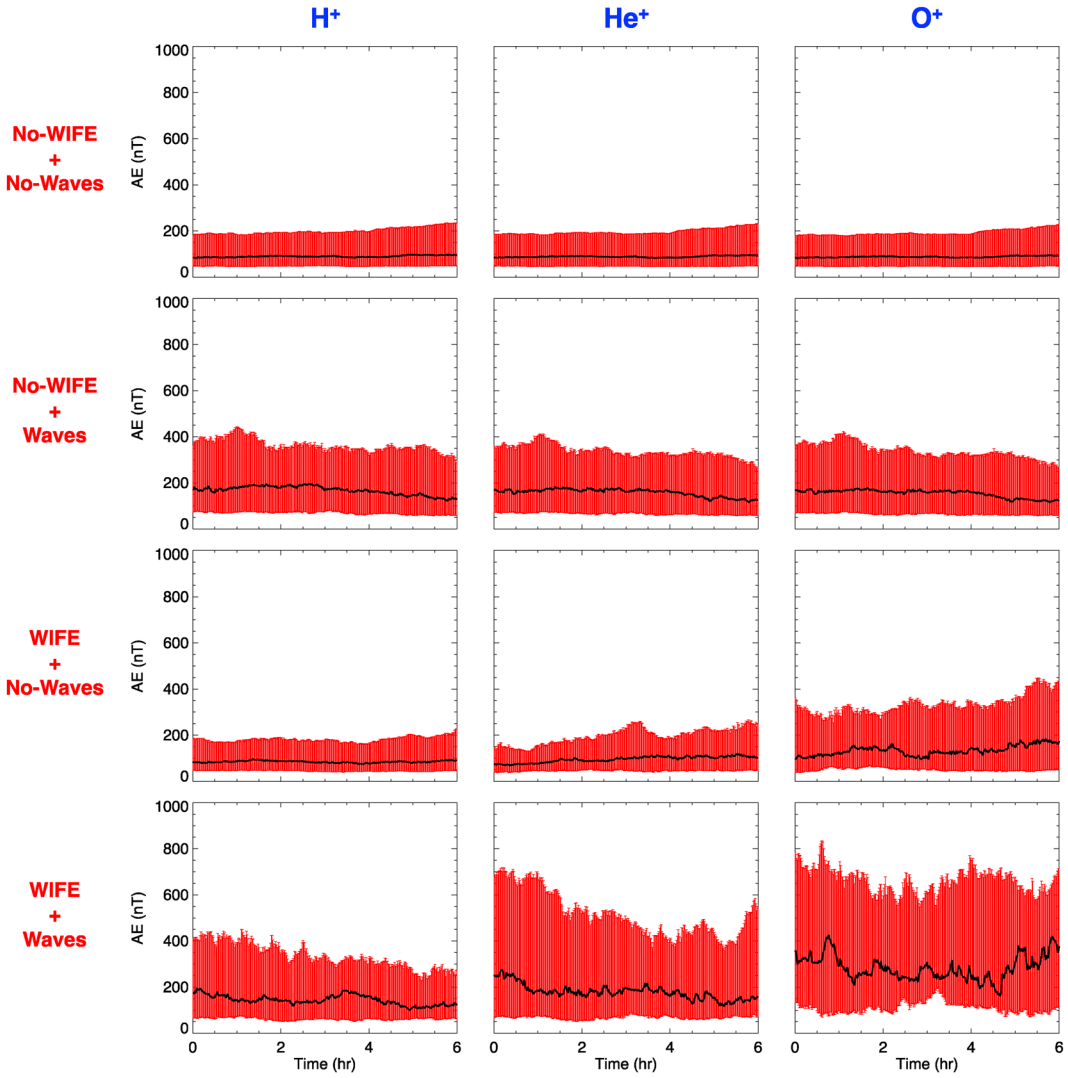

Figure 9. Superposed epoch analysis of the time history of the *AE* index during the 6 h prior to every density cavity event, organized by ion species and by the four types of events identified in Figure 7. The black curves are the median values and the red envelopes indicate the lower and upper quartiles.

The PADs of the cavity events with associated WIFE (two bottom rows in Figure 8) also show a clear species dependence. The warm H^+ fluxes have clear pancake PADs. Moreover, for the case when MS waves are present, the PAD is more strongly peaked at 90 and the peak flux is higher. The He^+ PADs with and without MS wave activity are qualitatively similar to those of H^+, that is, they have a strong perpendicular component and the peak flux is higher when waves are present. For O^+, the PADs are significantly different than for H^+ and He^+. The warm O^+ fluxes are observed mainly in the parallel and antiparallel directions forming a bidirectional distribution both in the presence and absence of MS waves. Similar to the lighter ions, when MS waves are present the O^+ peak flux is higher. Furthermore, a very weak component is observed in the perpendicular direction.

To provide context to the statistical results, we consider the history of geomagnetic activity for each of the four types of events identified in Figures 7 and 8. Since the history of the *Dst* index did not show any significant difference between the four groups, this analysis is not shown. Figure 9 shows a superposed epoch analysis of the history the *AE* index. Shown are the median, lower and upper quartiles of the *AE* index values during the 6 h prior to each event. The *AE* profiles are in general very similar for the three ion species when no WIFE was observed, with the profiles reaching higher values ($AE < 450$ nT) when MS waves are

present than when they are not present ($AE < 250$ nT). When WIFE was observed, the trends are that the AE profiles are most disturbed for O^+, then for He^+ and the least disturbed for H^+, and they are also more disturbed when MS waves are present than when they are not.

3. Discussion

In the present study, we perform a statistical study of the density cavities observed by RBSP-A over the four one-month periods of February and July 2013 and January and June 2014. Acknowledging that the cavities identified can be associated to a variety of density structures reported before, the large number of cavities found, 4,386, an average of approximately 14 cavities every orbit, indicates that these are common features in the inner magnetosphere during quiet and moderate conditions. This cavity occurrence rate is actually much higher than reported before for density cavities inside the plasmasphere. For example, in the survey of density structures using measurements from the Retarding Ion Mass Spectrometer (RIMS) onboard Dynamics Explorer 1, Horwitz et al. (1990) found that density profiles with troughs (patterns *D*, *E*, and *F* in their study), defined similarly as density depletions, were observed about 15% of the time. Using CRRES density measurements, Carpenter et al. (2000) found a relatively similar occurrence rate of 13%. The significantly higher occurrence rate found in this study is at least partly explained by two facts. First, while the above-mentioned studies restricted their analysis to density cavities inside the plasmasphere, we have not. In fact, as seen in Figure 7, a large fraction of the cavities observed in the EMFISIS data were outside the plasmasphere. Second, the criteria for cavity identification used in this study included a depletion factor that was less restrictive, namely 25%, than that used in the above-mentioned studies, namely 50%.

The MLT distribution of density cavities has shown that they were observed most often on the nightside, particularly in the MLT ~ 21-6 sector. This result is consistent with the statistical surveys of density structures by Horwitz et al. (1990) and by Carpenter et al. (2000). In their study, Horwitz et al. (1990) found that density profiles with troughs (patterns *D*, *E*, and *F* in their study) were observed primarily on the nightside, particularly in the premidnight quadrant. On the other hand, Carpenter et al. (2000) also found that the density trough occurrence rate was highest on the nightside, with slightly higher rate on the premidnight sector than in the postmidnight sector. Since density cavities most likely result from changes in magnetospheric convection during the last day or two prior to observation, we support the idea proposed by Horwitz et al. (1990) that the higher occurrence rate on the nightside might be indicative of a more variable convection pattern in this sector.

Previous studies of plasmaspheric structures concluded that the observed cavities are manifestations of field-aligned density depletions presumably caused by events during the time history of magnetospheric activity and convection, and appear as the signatures of plasma configurations previously established (e.g., Darrouzet et al., 2004; Kotova et al., 2004). Even though the connection can be established between the results reported here and the previous observations of density cavities, the main goal of this study is to report on the relationship between density cavities and WIFEs as observed by the Van Allen Probes.

To the best of the authors' knowledge, the statistical correlation between density cavities and WIFEs has not been reported before. As presented in the previous section, this correlation is species dependent, H^+ exhibiting the highest correlation (20%), then He^+ (6%) and finally O^+ (4%). We also noted a different trend in the cavity-WIFE correlation between the lighter ions (H^+ and He^+) and O^+. Even though geomagnetic activity was relatively low during three of the four months studied and thus it is not expected that there will be a clear, well-defined plasmapause throughout these periods, we decided to use a density criterion for the plasmapause location as a general proxy for the cavity observations. If using this criterion, we only consider the cavities observed inside the plasmasphere, the cavity-WIFE correlation increases for H^+ and He^+ (28% for H^+ and 9% for He^+) but remains the same for O^+ (4%). Moreover, considering the preferred location of WIFE events, we find that 76% of cavities with associated H^+ and He^+ WIFEs were observed inside the plasmasphere, whereas 57% of cavities with associated O^+ WIFEs were observed inside the plasmasphere. This species dependence of the cavity-WIFE correlation and the different trend between the lighter ions and O^+ are qualitatively consistent with the relative abundances of the three ion species in the plasmasphere as indicated by the cold ion densities observed by the RIMS instrument (Goldstein et al., 2019). Goldstein et al. (2019) compiled results from the DE-1 mission and showed that the lighter ions, H^+ and He^+, have

very similar density and temperature radial distributions, whereas the distributions of O^+ are strikingly different. They also found that the He^+ density is, on average, 10%–20% of the H^+ density, and the O^+ density is overall one or two orders of magnitude lower than the H^+ density. These results are also consistent with Cluster observations of the ion composition of the plasmasphere (Dandouras et al., 2005).

The species dependence of the correlation between observations of density cavities and WIFEs, particularly the better correlation with H^+, and the observed enhanced fluxes in the direction perpendicular to the magnetic field for H^+ and He^+ suggest a cold ion heating mechanism such as heating by interaction with MS waves. Recent studies have reported events where MS waves and WIFE were observed concurrently. The study by Yuan et al. (2018) reported observations of an event where warm H^+ and He^+ transverse flux enhancements were observed concurrent with a density cavity and MS wave activity, and it was interpreted as cold ion heating by MS waves. Ma et al. (2019) also reported an event of H^+ WIFE and using simulations concluded that it was caused by heating of cold H^+ by MS waves inside a density cavity. On the other hand, a recent study has reported the modulation of MS waves by density structures, where the MS waves were instead observed on the high-density regions of the cavities; they concluded that unstable H^+ at hundreds of eV generated the MS waves in the high-density region (Yue et al., 2020). Moreover, another recent study has shown observational evidence of cold O^+ heating by MS waves exhibiting heavy ion gyro-harmonics inside a density cavity (Hill et al., 2020).

Despite the possibility for the cause-effect relationship between MS waves and a fraction of the H^+ and He^+ WIFEs, the majority of the H^+ and He^+ WIFE events (82% for H^+ and 74% for He^+) are not associated with direct observation of these waves. The H^+ and He^+ PADs in Figure 8 show that the flux enhancements in absence of MS waves were weaker but also occurred mainly in the perpendicular direction. It could be the case that MS waves caused the heating of cold ions in some other region of the cavity, for example closer to the magnetic equator, with their effects on the plasma being observed at higher latitudes even though the waves themselves were not observed directly. Another possibility could be that the MS waves caused the ion heating and then disappeared due to the transfer of energy from the waves to the plasma. Still, the fact that the majority of WIFE events are not concurrent with the observation of MS waves suggests that cold ion heating by this type of wave is not the main cause for the observed H^+ and He^+ WIFEs.

In this study we have focused on the statistical correlation between density cavities with concurrent WIFEs and MS waves motivated by the recent case studies that showed that MS waves can heat cold ions inside density cavities producing WIFEs (e.g., Hill et al., 2020; Ma et al., 2019). However, there are other types of waves that could produce transverse cold ion heating by resonant interaction. Such waves include electromagnetic ion cyclotron (EMIC) waves, although it is understood that EMIC waves preferentially grow in regions of high density and not in low-density cavities (de Soria-Santacruz et al., 2013; Fraser et al., 2005; Horne & Thorne, 1997; Zhang et al., 2010). The role of EMIC waves in producing the observed WIFE events will be subject of future investigation. Another possible explanation for the density cavities with associated WIFE is that these cavities are the signatures of mixing of plasma from different populations. In the case of density cavities with concurrent H^+ and He^+ WIFEs, it could be that the density cavities contain warm ions that once were on open drift trajectories accessible from the tail plasma sheet. The plasma sheet, having particles with typical energies of a few keV, can often exhibit a colder component of ions with energies of ~10 eV or even less in the near-Earth central plasma sheet (e.g., Borovsky et al., 1997; Ebihara et al., 2008; Seki et al., 2003). The drift motion into the inner magnetosphere, and losses suffered along the way due to charge exchange and Coulomb collisions, would make the PADs more perpendicular at the same time that the ions gain energy adiabatically. Two recent studies have reported warm ion "finger" structures observed by the Van Allen Probes during storm times, which were rich in He^+ and/or O^+ (Denton et al., 2016; Wang et al., 2020). These finger structures have characteristic energies of tens of eV to a few keV and, as seen in the energy-time spectrograms, they look similar to the WIFE events reported here. Using particle drift tracing, these structures were interpreted as being formed by warm ions of tail plasma sheet origin that drifted into the inner magnetosphere by enhanced convection. However, the WIFE events reported here are observed more often and with higher fluxes for H^+ and are not necessarily associated with strong convection, thus a formation mechanism such as for the finger structures seems unlikely.

On the other hand, there is plenty of evidence from early missions, such as ATS-6, SCATHA and ISEE-1, that there is a warm component of trapped ions in the outer plasmasphere and plasma trough regions (e.g.,

Horwitz & Chappell, 1979; Horwitz et al., 1981; Olsen, 1981; Quinn & Johnson, 1982). In fact, this warm plasma population exhibits complex PADs, including various combinations of pancake, field-aligned, and conical components (Horwitz & Chappell, 1979). For example, using measurement made with the SCATHA mission, Reasoner et al. (1983) reported the observation of cold ions intertwined with warm trapped and warm field-aligned ions, and using data from the ISEE-1 mission, Horwitz et al. (1981) showed species-dependent PADs in the same flux tube, namely field-aligned H^+, pancake He^+, and isotropic O^+.

If, as several studies suggest, the density cavities are product of previous plasma configurations, flux tubes containing warm plasma from the plasma cloak or the plasma trough could get mixed with colder corotating plasma after some change in convection moves the boundary of corotating plasma outward. In light of previous observations of mixed PADs in the same flux tube in the outer plasmaspheric and trough regions, and from the results presented here, it seems likely that mixing and intertwining of plasma from different populations is the mechanism or process responsible for the concurrent observations of H^+ and He^+ WIFE and density cavities. Additional analysis is needed to confirm this.

The bidirectional PADs of the O^+ WIFE events with and without concurrent observations of MS waves, on the other hand, are not consistent with the interaction with MS waves, which heats the plasma in the transverse direction. It should be noted, however, that there is a weak perpendicular component of O^+ WIFE when MS waves are present. Cold O^+ heating by MS waves as an explanation for these events would be consistent with recent findings (Hill et al., 2020). A recent study by Hill et al. (2020) presented three cavity events with associated observation of MS wave activity and O^+ WIFE and they showed that the WIFE was caused by MS wave heating. Similar case studies would be needed to further examine the relationship between MS waves and O^+ WIFE. The measured predominantly bidirectional PADs during O^+ WIFE events are consistent with previous studies of the warm plasma cloak (e.g., Chappell et al., 2008; Nagai et al., 1983; Yue et al., 2017). Chappell et al. (2008) described the energy of the O^+ plasma cloak to be in the range of a few eV to a few keV and suggested that this population is formed by ions of ionospheric origin that are accelerated in the polar wind across the polar cap, out to the magnetotail and back to the middle magnetosphere where they are confined to the region outside the plasmasphere. A mixing of warm plasma cloak O^+ with the colder plasma from the plasmasphere, in a scenario of changing convection as described above, seems like a likely explanation for the density cavities with concurrent O^+ WIFE. Further investigation, including particle tracing, is needed to determine the cause for the WIFEs, and this will be subject of future work.

4. Summary

The plasma observations presented here provide new insight on the density cavities and ion populations in the inner magnetosphere. The main findings of this study can be summarized as follows.

1. Density cavities were found to be a common feature of the inner magnetosphere during periods of quiet to moderate geomagnetic activity, with an average occurrence rate of ~14 cavities per orbit of RBSP-A
2. Around half of the density cavities (52%) were observed inside the plasmasphere, with a higher occurrence rate of density cavities on the nightside, between MLT = 21–6
3. Concurrent with the observation of the density cavities, WIFEs at energies of 10–100 eV were observed and exhibited a clear species dependence: a preferred occurrence for H^+ (20%), then for He^+ (6%), and then for O^+ (4%). Moreover, the lighter ions exhibited a similar, preferred occurrence inside the plasmasphere, whereas O^+ did not. The H^+ and He^+ WIFE occurrence rates were increased when considering only the cavities inside the plasmasphere, to 28% for H^+ and 9% for He^+, whereas the occurrence rate remained at 4% for O^+. Furthermore, 76% of H^+ and He^+ WIFEs where detected inside the plasmasphere, while for O^+ only 57%
4. Most concurrent observations of density cavities and WIFEs were not associated with the direct observation of MS wave activity, that is 82% of the H^+ WIFE events, and 74% and 81% of the He^+ and O^+ WIFE events, respectively
5. When MS waves were observed concurrently with WIFE events, the H^+ and He^+ PADs show enhanced transverse fluxes and the O^+ PADs exhibit a predominantly bidirectional flux enhancement with a weak enhancement in the transverse direction. This seems to be consistent with the finding of Hill et al. (2020) that MS wave heating affects H^+ first, then He^+, and finally O^+. However, even though cold ion heating by interaction with MS waves cannot be discarded as a possible mechanism responsible for some

observed WIFE events, the results from this study suggest that it is not the main cause for the observed WIFEs. The mixing of plasma from different plasma populations, like the plasmasphere, trough and cloak, resulting from the intertwining of flux tubes after periods of changing convection seems like a probable explanation for the concurrent observation of density cavities and WIFE

6. The warm ion PADs of the cavity events without concurrent WIFE indicate that different ion species with warm plasma energies can have very different PADs, H^+ exhibiting bidirectional distributions with a weaker perpendicular component, He^+ exhibiting a bidirectional component accompanied by a stronger perpendicular component, and O^+ showing bidirectional distributions

Data Availability Statement

The authors would like to acknowledge the Van Allen Probes EMFISIS, EFW, and HOPE teams for providing the data utilized in this study and Jerry Goldstein for useful discussions. HOPE data used in this paper are available from the Van Allen Probes ECT website at http://www.rbsp-ect.lanl.gov/rbsp_ect.php. EMFISIS and EFW data used are available at NASA's Coordinated Data Analysis Web (CDAWeb) website at https://cdaweb.gsfc.nasa.gov/. The *AE* indices were obtained from the GSFC/SPDF OMNIWeb interface at http://omniweb.gsfc.nasa.gov. The tables containing the lists of density cavity events and the associated warm ion flux enhancements are publicly available at https://doi.org/10.6084/m9.figshare.13693162.v1.

Acknowledgments
This work was supported by the NASA Heliophysics Living With a Star Science program, under Work Breakdown Structure 936,723.02.01.11.18. Work at LANL was performed under the auspices of the United States Department of Energy.

References

Baugher, C. R., Chappell, C. R., Horwitz, J. L., Shelley, E. G., & Young, D. T. (1980). Initial thermal plasma observations from ISEE-1. *Geophysical Research Letters*, *7*(9), 657–660. https://doi.org/10.1029/GL007i009p00657

Boardsen, S. A., Gallagher, D. L., Gurnett, D. A., Peterson, W. K., & Green, J. L. (1992). Funnel-shaped, low-frequency equatorial waves. *Journal of Geophysical Research*, *97*(A10), 14967. https://doi.org/10.1029/92ja00827

Boardsen, S. A., Hospodarsky, G. B., Kletzing, C. A., Engebretson, M. J., Pfaff, R. F., Wygant, J. R., et al. (2016). Survey of the frequency dependent latitudinal distribution of the fast magnetosonic wave mode from Van Allen Probes electric and magnetic field instrument and integrated science waveform receiver plasma wave analysis. *Journal of Geophysical Research: Space Physics*, *121*(4), 2902–2921. https://doi.org/10.1002/2015JA021844

Borovsky, J. E., Thomsen, M. F., & McComas, D. J. (1997). The superdense plasma sheet: Plasmaspheric origin, solar wind origin, or ionospheric origin? *Journal of Geophysical Research: Space Physics*, *102*(A10), 22089–22097. https://doi.org/10.1029/96JA02469

Bortnik, J., & Thorne, R. M. (2010). Transit time scattering of energetic electrons due to equatorially confined magnetosonic waves. *Journal of Geophysical Research*, *115*(A7). https://doi.org/10.1029/2010ja015283

Burch, J. L., Goldstein, J., & Sandel, B. R. (2004). Cause of plasmasphere corotation lag. *Geophysical Research Letters*, *31*(5). https://doi.org/10.1029/2003gl019164

Carpenter, D. L., Anderson, R. R., Calvert, W., & Moldwin, M. B. (2000). CRRES observations of density cavities inside the plasmasphere. *Journal of Geophysical Research: Space Physics*, *105*(A10), 23323–23338. https://doi.org/10.1029/2000ja000013

Carpenter, D. L., & Lemaire, J. (2004). The plasmasphere boundary layer. *Annales Geophysicae*, *22*, 4291–4298. https://doi.org/10.5194/angeo-22-4291-2004

Chappell, C. R. (1982). Low energy particles in the magnetosphere. *Advances in Space Research*, *2*(1), 33–38. https://doi.org/10.1016/0273-1177(82)90089-8

Chappell, C. R., Huddleston, M. M., Moore, T. E., Giles, B. L., & Delcourt, D. C. (2008). Observations of the warm plasma cloak and an explanation of its formation in the magnetosphere. *Journal of Geophysical Research: Space Physics*, *113*(A9). https://doi.org/10.1029/2007JA012945

Chen, L., Thorne, R. M., Jordanova, V. K., Thomsen, M. F., & Horne, R. B. (2011). Magnetosonic wave instability analysis for proton ring distributions observed by the LANL magnetospheric plasma analyzer. *Journal of Geophysical Research: Space Physics*, *116*(A3). https://doi.org/10.1029/2010JA016068

Dandouras, I., Pierrard, V., Goldstein, J., Vallat, C., Parks, G. K., Rème, H., et al. (2005). Multipoint observations of ionic structures in the plasmasphere by CLUSTER—CIS and comparisons with IMAGE-EUV observations and with model simulations. In Inner magnetosphere interactions: New perspectives from imaging (159, pp. 23–53). New York, NY: Wiley Blackwell. https://doi.org/10.1029/159GM03

Darrouzet, F., Décréau, P. M. E., De Keyser, J., Masson, A., Gallagher, D. L., Santolik, O., et al. (2004). Density structures inside the plasmasphere: Cluster observations. *Annales Geophysicae*, *22*(7), 2577–2585. https://doi.org/10.5194/angeo-22-2577-2004

Darrouzet, F., Gallagher, D. L., André, N., Carpenter, D. L., Dandouras, I., Décréau, P. M. E., et al. (2009). Plasmaspheric density structures and dynamics: Properties observed by the CLUSTER and IMAGE missions. *Space Science Reviews*, *145*(1–2), 55–106. https://doi.org/10.1007/s11214-008-9438-9

Denton, M. H., Reeves, G. E., Thomsen, M. F., Henderson, M. G., Friedel, R. H. W., Larsen, B., et al. (2016). The complex nature of storm-time ion dynamics: Transport and local acceleration. *Geophysical Research Letters*, *43*(19), 10059–10067. https://doi.org/10.1002/2016GL070878

de Soria-Santacruz, M., Spasojevic, M., & Chen, L. (2013). EMIC waves growth and guiding in the presence of cold plasma density irregularities. *Geophysical Research Letters*, *40*(10), 1940–1944. https://doi.org/10.1002/grl.50484

Ebihara, Y., Kistler, L. M., & Eliasson, L. (2008). Imaging cold ions in the plasma sheet from the Equator-S satellite. *Geophysical Research Letters*, *35*(15), L15103. https://doi.org/10.1029/2008GL034357

Fraser, B. J., Singer, H. J., Adrian, M. L., Gallagher, D. L., & Thomsen, M. F. (2005). The relationship between plasma density structure and EMIC waves at geosynchronous orbit. *Advancing Earth and Space Science*, *159*, 55–70. https://doi.org/10.1029/159GM04

Funsten, H. O., Skoug, R. M., Guthrie, A. A., MacDonald, E. A., Baldonado, J. R., Harper, R. W., et al. (2013). Helium, oxygen, proton, and electron (HOPE) mass spectrometer for the radiation belt storm probes mission. *Space Science Reviews*, *179*, 423–484. https://doi.org/10.1007/978-1-4899-7433-4-13

Gallagher, D. L., Adrian, M. L., & Liemohn, M. W. (2005). Origin and evolution of deep plasmaspheric notches. *Journal of Geophysical Research: Space Physics*, *110*(A9), 1–11. https://doi.org/10.1029/2004JA010906

Goldstein, J., Gallagher, D., Craven, P. D., Comfort, R. H., Genestreti, K. J., Mouikis, C., et al. (2019). Temperature dependence of plasmaspheric ion composition. *Journal of Geophysical Research: Space Physics*, *124*(8), 6585–6595. https://doi.org/10.1029/2019JA026822

Goldstein, J., Thomsen, M. F., & DeJong, A. (2014). In situ signatures of residual plasmaspheric plumes: Observations and simulation. *Journal of Geophysical Research: Space Physics*, *119*(6), 4706–4722. https://doi.org/10.1002/2014JA019953

Gurgiolo, C., Sandel, B. R., Perez, J. D., Mitchell, D. G., Pollock, C. J., & Larsen, B. A. (2005). Overlap of the plasmasphere and ring current: Relation to subauroral ionospheric heating. *Journal of Geophysical Research*, *110*(A12), A12217. https://doi.org/10.1029/2004JA010986

Hartley, D. P., Kletzing, C. A., Kurth, W. S., Bounds, S. R., Averkamp, T. F., Hospodarsky, G. B., et al. (2016). Using the cold plasma dispersion relation and whistler mode waves to quantify the antenna sheath impedance of the Van Allen Probes EFW instrument. *Journal of Geophysical Research: Space Physics*, *121*(5), 4590–4606. https://doi.org/10.1002/2016JA022501

Hill, S., Buzulukova, N., Boardsen, S., & Fok, M.-C. (2020). Local heating of oxygen ions in the presence of magnetosonic waves: Possible source for the warm plasma cloak? *Journal of Geophysical Research: Space Physics*, *125*(8), 1–23. https://doi.org/10.1029/2019JA027210

Horne, R. B., & Thorne, R. M. (1997). Wave heating of He^+ by electromagnetic ion cyclotron waves in the magnetosphere: Heating near the H^+-He^+ bi-ion resonance frequency. *Journal of Geophysical Research - A: Space Physics*, *102*(A6), 11457–11471. https://doi.org/10.1029/97ja00749

Horne, R. B., Wheeler, G. V., & Alleyne, H. S. C. K. (2000). Proton and electron heating by radially propagating fast magnetosonic waves. *Journal of Geophysical Research: Space Physics*, *105*(A12), 27597–27610. https://doi.org/10.1029/2000JA000018

Horwitz, J. L., Baugher, C. R., Chappell, C. R., Shelley, E. G., & Young, D. T. (1981). Pancake pitch angle distributions in warm ions observed with ISEE 1. *Journal of Geophysical Research*, *86*(A5), 3311–3320. https://doi.org/10.1029/ja086ia05p03311

Horwitz, J. L., & Chappell, C. R. (1979). Observations of warm plasma in the dayside plasma trough at geosynchronous orbit. *Journal of Geophysical Research*, *84*(A12), 7075–7090. https://doi.org/10.1029/ja084ia12p07075

Horwitz, J. L., Comfort, R. H., & Chappell, C. R. (1990). A statistical characterization of plasmasphere density structure and boundary locations. *Journal of Geophysical Research*, *95*(A6), 7937–7947. https://doi.org/10.1029/ja095ia06p07937

Kletzing, C. A., Kurth, W. S., Acuna, M., MacDowall, R. J., Torbert, R. B., Averkamp, T., et al. (2013). The electric and magnetic field instrument suite and integrated science (EMFISIS) on RBSP. *Space Science Reviews*, *179*, 127–181. https://doi.org/10.1007/s11214-013-9993-6

Kotova, G., Bezrukikh, V., Verigin, M., & Smilauer, J. (2004). In situ observations of low-density regions inside the plasmasphere. *Earth Planets and Space*, *56*(10), 989–996. https://doi.org/10.1186/BF03351796

Laakso, H., Junginger, H., Roux, A., Schmidt, R., & de Villedary, C. (1990). Magnetosonic waves above f_c (H^+) at geostationary orbit: GEOS 2 results. *Journal of Geophysical Research*, *95*(A7), 10609. https://doi.org/10.1029/ja095ia07p10609

Lennartsson, W., & Reasoner, D. L. (1978). Low-energy plasma observations at synchronous orbit. *Journal of Geophysical Research*, *83*(A5), 2145–2156. https://doi.org/10.1029/ja083ia05p02145

Li, W., Thorne, R. M., Bortnik, J., Nishimura, Y., Angelopoulos, V., Chen, L., et al. (2010). Global distributions of suprathermal electrons observed on THEMIS and potential mechanisms for access into the plasmasphere. *Journal of Geophysical Research: Space Physics*, *115*(12). https://doi.org/10.1029/2010JA015687

Ma, Q., Li, W., Chen, L., Thorne, R. M., Kletzing, C. A., Kurth, W. S., et al. (2014). The trapping of equatorial magnetosonic waves in the Earth's outer plasmasphere. *Geophysical Research Letters*, *41*(18), 6307–6313. https://doi.org/10.1002/2014GL061414

Ma, Q., Li, W., Yue, C., Thorne, R. M., Bortnik, J., Kletzing, C. A., et al. (2019). Ion heating by electromagnetic ion cyclotron waves and magnetosonic waves in the Earth's inner magnetosphere. *Geophysical Research Letters*, *46*, 6258–6267. https://doi.org/10.1029/2019GL083513

Mauk, B. H., Fox, N. J., Kanekal, S. G., Kessel, R. L., Sibeck, D. G., & Ukhorskiy, A. (2013). Science objectives and rationale for the radiation belt storm probes mission. *Space Science Reviews*, *179*, 3–27. https://doi.org/10.1007/978-1-4899-7433-4-2

Moldwin, M. B., Thomsen, M. F., Bame, S. J., McComas, D., & Reeves, G. D. (1995). The fine-scale structure of the outer plasmasphere. *Journal of Geophysical Research*, *100*(A5), 8021–8029. https://doi.org/10.1029/94ja03342

Moldwin, M. B., Thomsen, M. F., Bame, S. J., McComas, D. J., & Moore, K. R. (1994). An examination of the structure and dynamics of the outer plasmasphere using multiple geosynchronous satellites. *Journal of Geophysical Research*, *99*(A6), 11475. https://doi.org/10.1029/93ja03526

Mouikis, C. G., Kistler, L. M., Baumjohann, W., Lund, E. J., Korth, A., Klecker, B., et al. (2002). Equator-S observations of He^+ energization by EMIC waves in the dawnside equatorial magnetosphere. *Geophysical Research Letters*, *29*(10). https://doi.org/10.1029/2001GL013899

Mourenas, D., Artemyev, A. V., Agapitov, O. V., & Krasnoselskikh, V. (2013). Analytical estimates of electron quasi-linear diffusion by fast magnetosonic waves. *Journal of Geophysical Research: Space Physics*, *118*(6), 3096–3112. https://doi.org/10.1002/jgra.50349

Nagai, T., Johnson, J. F. E., & Chappell, C. R. (1983). Low-energy (<100 eV) ion pitch angle distributions in the magnetosphere by ISEE 1. *Journal of Geophysical Research*, *88*(A9), 6944. https://doi.org/10.1029/JA088iA09p06944

Olsen, R. C. (1981). Equatorially trapped plasma populations. *Journal of Geophysical Research*, *86*(A13), 11235. https://doi.org/10.1029/JA086iA13p11235

Olsen, R. C., Scott, L. J., & Boardsen, S. A. (1994). Comparison between Liouville's theorem and observed latitudinal distributions of trapped ions in the plasmapause region. *Journal of Geophysical Research*, *99*(A2), 2191–2203. https://doi.org/10.1029/93ja02776

Perraut, S., Roux, A., Robert, P., Gendrin, R., Sauvaud, J.-A., Bosqued, J.-M., et al. (1982). A systematic study of ULF Waves Above FH+ from GEOS 1 and 2 measurements and their relationships with proton ring distributions. *Journal of Geophysical Research*, *87*(A8), 6219. https://doi.org/10.1029/ja087ia08p06219

Pierrard, V., & Cabrera, J. (2005). Comparisons between EUV/IMAGE observations and numerical simulations of the plasmapause formation. *Annales Geophysicae*, *23*(7), 2635–2646. https://doi.org/10.5194/angeo-23-2635-2005

Quinn, J. M., & Johnson, R. G. (1982). Composition measurements of warm equatorially trapped ions near geosynchronous orbit. *Geophysical Research Letters*, *9*(7), 777–780. https://doi.org/10.1029/GL009i007p00777

Reasoner, D. L., Craven, P. D., & Chappell, C. R. (1983). Characteristics of low-energy plasma in the plasmasphere and plasma trough. *Journal of Geophysical Research*, *88*(A10), 7913–7925. https://doi.org/10.1029/JA088iA10p07913

Santolík, O., Němec, F., Gereová, K., Macúšová, E., de Conchy, Y., & Cornilleau-Wehrlin, N. (2004). Systematic analysis of equatorial noise below the lower hybrid frequency. *Annales Geophysicae*, *22*, 2587–2595. https://doi.org/10.5194/angeo-22-2587-2004

Santolík, O., Pickett, J. S., Gurnett, D. A., Maksimovic, M., & Cornilleau-Wehrlin, N. (2002). Spatiotemporal variability and propagation of equatorial noise observed by Cluster. *Journal of Geophysical Research: Space Physics*, *107*(A12), 1–8. https://doi.org/10.1029/2001JA009159

Sarno-Smith, L. K., Larsen, B. A., Skoug, R. M., Liemohn, M. W., Breneman, A., Wygant, J. R., & Thomsen, M. F. (2016). Spacecraft surface charging within geosynchronous orbit observed by the Van Allen Probes. *Space Weather*, *14*(2), 151–164. https://doi.org/10.1002/2015SW001345

Seki, K., Hirahara, M., Hoshino, M., Terasawa, T., Elphic, R. C., Saito, Y., et al. (2003). Cold ions in the hot plasma sheet of Earth's magnetotail. *Nature*, *422*(6932), 589–592. https://doi.org/10.1038/nature01502

Sheeley, B. W., Moldwin, M. B., Rassoul, H. K., & Anderson, R. R. (2001). An empirical plasmasphere and trough density model: CRRES observations. *Journal of Geophysical Research: Space Physics*, *106*(A11), 25631–25641. https://doi.org/10.1029/2000ja000286

Spasojević, M. (2003). Global response of the plasmasphere to a geomagnetic disturbance. *Journal of Geophysical Research*, *108*(A9), 1340. https://doi.org/10.1029/2003JA009987

Spence, H. E., Reeves, G. D., Baker, D. N., Blake, J. B., Bolton, M., Bourdarie, S., et al. (2013). Science goals and overview of the radiation belt storm probes (RBSP) energetic particle, composition, and thermal plasma (ECT) suite on NASA's Van Allen Probes mission. *Space Science Reviews*, 311–336. https://doi.org/10.1007/978-1-4899-7433-4-10

Sun, J., Gao, X., Lu, Q., Chen, L., Liu, X., Wang, X., et al. (2017). Spectral properties and associated plasma energization by magnetosonic waves in the Earth's magnetosphere: Particle-in-cell simulations. *Journal of Geophysical Research: Space Physics*, *122*(5), 5377–5390. https://doi.org/10.1002/2017JA024027

Thomsen, M. F., Denton, M. H., Jordanova, V. K., Chen, L., & Thorne, R. M. (2011). Free energy to drive equatorial magnetosonic wave instability at geosynchronous orbit. *Journal of Geophysical Research: Space Physics*, *116*(A8). https://doi.org/10.1029/2011JA016644

Tsyganenko, N. A., & Sitnov, M. I. (2005). Modeling the dynamics of the inner magnetosphere during strong geomagnetic storms. *Journal of Geophysical Research: Space Physics*, *110*(A3), 1–16. https://doi.org/10.1029/2004JA010798

Wang, Y. B., Kistler, L. M., Mouikis, C. G., Zhang, J. C., Lu, J. Y., Welling, D., et al. (2020). Formation of the low-energy "Finger" ion spectral structure near the inner edge of the plasma sheet. *Geophysical Research Letters*, *47*(22). https://doi.org/10.1029/2020GL089875

Xiao, F., Zong, Q., Wang, Y., He, Z., Su, Z., Yang, C., & Zhou, Q. (2014). Generation of proton aurora by magnetosonic waves. *Scientific Reports*, *4*(1), 1–7. https://doi.org/10.1038/srep05190

Young, D. T., Perraut, S., Roux, A., de Villedary, C., Gendrin, R., Korth, A., et al. (1981). Wave-particle interactions near ΩHe+ observed on GEOS 1 and 2 1. Propagation of ion cyclotron waves in He^+ -rich plasma. *Journal of Geophysical Research*, *86*(A8), 6755–6772. https://doi.org/10.1029/JA086iA08p06755

Yuan, Z., Yu, X., Huang, S., Qiao, Z., Yao, F., & Funsten, H. O. (2018). Cold ion heating by magnetosonic waves in a density cavity of the plasmasphere. *Journal of Geophysical Research: Space Physics*, *123*. https://doi.org/10.1002/2017JA024919

Yuan, Z., Yu, X., Huang, S., Wang, D., & Funsten, H. O. (2017). In situ observations of magnetosonic waves modulated by background plasma density. *Geophysical Research Letters*, *44*(15), 7628–7633. https://doi.org/10.1002/2017GL074681

Yue, C., Bortnik, J., Thorne, R. M., Ma, Q., An, X., Chappell, C. R., et al. (2017). The characteristic pitch angle distributions of 1 eV to 600 keV protons near the equator based on Van Allen Probes observations. *Journal of Geophysical Research: Space Physics*, *122*(9), 9464–9473. https://doi.org/10.1002/2017JA024421

Yue, C., Ma, Q., Jun, C.-W., Bortnik, J., Jang, E., Zong, Q., et al. (2020). The modulation of plasma and waves by the background electron density irregularitiy in the inner magnetosphere. *Journal of Geophysical Research: Space Physics*, *47*(15), e2020GL088855. https://doi.org/10.1029/2020GL088855

Zhang, J.-C., Kistler, L. M., Mouikis, C. G., Dunlop, M. W., Klecker, B., & Sauvaud, J.-A. (2010). A case study of EMIC wave-associated He energization in the outer magnetosphere: Cluster and Double Star 1 observations. *Journal of Geophysical Research*, *115*(A6), A06212. https://doi.org/10.1029/2009JA014784

Zhang, J.-C., Kistler, L. M., Mouikis, C. G., Klecker, B., Sauvaud, J.-A., & Dunlop, M. W. (2011). A statistical study of EMIC wave-associated He^+ energization in the outer magnetosphere: Cluster/CODIF observations. *Journal of Geophysical Research*, *116*(A11), A11201. https://doi.org/10.1029/2011JA016690